

Article

Injection Flow Rate Threshold Preventing Atypical In-Cavity Pressure during Low-Pressure Powder Injection Molding

Francis Arès, Dorian Delbergue  and Vincent Demers * 

École de Technologie Supérieure, 1100 Notre-Dame West, Montreal, QC H3C 1K3, Canada; francis.ares.1@ens.etsmtl.ca (F.A.); dorian.delbergue.1@ens.etsmtl.ca (D.D.)

* Correspondence: vincent.demers@etsmtl.ca; Tel.: +1-514-396-8590

Abstract: Controlling injection parameters is paramount when it comes to producing high-quality green parts using powder injection molding. This work combines experimental and numerical approaches to study the impact of injection parameters on mold in-cavity pressure and on the overall quality of green parts produced by low-pressure powder injection molding. The properties of two low-viscosity feedstocks (formulated from a water-atomized stainless-steel powder and wax-based binder system) were measured and implemented in an Autodesk Moldflow numerical model to quantify the molding pressures, which were finally validated using experimental real-scale injections. The results confirmed that an increase in mold temperature, an increase in feedstock temperature, and a decrease in solid loading decrease the mold in-cavity pressure, which was correlated with the feedstock viscosity. As a key result, real-scale injections confirmed that a minimum flow rate was required to avoid atypical high in-cavity pressure leading to several visual defects such as weld lines, flow marks, cracks, sinks, and incomplete filling. Due to differences in its thermal transfer properties, this flow rate threshold value decreases as the feedstock solid loading increases. For injection speeds higher than this value, the injection pressure measured experimentally was linearly correlated with the injection flow rate.

Keywords: low-pressure powder injection molding; metallic powder; numerical simulation; injection pressure



Citation: Arès, F.; Delbergue, D.; Demers, V. Injection Flow Rate Threshold Preventing Atypical In-Cavity Pressure during Low-Pressure Powder Injection Molding. *Powders* **2023**, *2*, 709–726. <https://doi.org/10.3390/powders2040044>

Academic Editor: Paul F. Luckham

Received: 26 May 2023

Revised: 3 October 2023

Accepted: 1 November 2023

Published: 7 November 2023



Copyright: © 2023 by the authors. Licensee MDPI, Basel, Switzerland. This article is an open access article distributed under the terms and conditions of the Creative Commons Attribution (CC BY) license (<https://creativecommons.org/licenses/by/4.0/>).

1. Introduction

Metal injection molding (MIM) is a manufacturing process suitable for producing complex shape and small metallic parts within reasonable dimensional tolerances, especially when other conventional processes have reached their technical limits or become too expensive [1]. The MIM process can be divided into four steps, namely, feedstock preparation, injection molding, debinding, and sintering [2]. Although each of these steps must be properly executed, the injection molding parameters must be controlled in order to produce high-quality green parts [3]. Depending on the binder formulation driving the final feedstock viscosity, the injection stage can be performed using either a high-pressure injection molding (HPIM) or a low-pressure injection molding (LPIM) approach [4]. One of the main differences between these two techniques lies in the size of the injection molding equipment used. In HPIM, the injection unit is composed of a reciprocating screw mechanism rotating in a heated barrel to transport a high-viscosity feedstock (e.g., >100 Pa·s, at a temperature above 160 °C) that is injected into a cooled mold cavity using a translation movement of the same screw to produce an injection pressure generally higher than 50 MPa [5]. In LPIM, on the other hand, the injection unit consists of an air-pressurized container [6] or a plunger system [7] used to transport a low-viscosity feedstock (e.g., <20 Pa·s, at a temperature below 100 °C) that is injected into an air-cooled mold cavity using an injection pressure generally lower than 1 MPa [8]. While the latter injection approach is still in its infancy, it is a promising manufacturing technology for producing

metallic parts cost-effectively either in low- or in high-production volumes thanks to the simplicity of its underlying principle and the reduction in the size of the machines and mold shells involved.

As ceramic-based LPIM feedstock development pioneers, Mangels and Williams [9] were among the first to demonstrate the high moldability of such low-viscosity feedstocks. Approximately ten years later, the same research team confirmed that the pressurized container principle developed by Peltzman Corp. [10] was able to produce ceramic green parts exhibiting a very high level of shape complexity, using high solid loading feedstocks [11]. In the early 2000s, Gonçalves [12] showed that this injection approach could even be used for conventional high-viscosity metallic-based feedstocks. However, the study concluded that a process needed to be developed specifically to better understand the interaction between injection variables and to mitigate problems appearing during debinding. Almost simultaneously, Quevedo Nogueira et al. [13] demonstrated that carnauba wax could be successfully used as an organic vehicle in the formulation of low-viscosity ceramic-based feedstock and injected at a pressure as low as 0.6 MPa when blended with low-density polyethylene and stearic acid. Ten years later, in a very comprehensive study, Piotter et al. [14] confirmed the ability of the LPIM process to produce microscopic parts (also known as micro-PIM) from ceramic- as well as metallic-based feedstocks. Using a ceramic-based feedstock, Çetinel et al. [15] studied material- and process-related factors in a bid to improve shape retention and bending strength after the debinding/sintering stages. More recently, Medvedovski and Peltsman [16] and Sardarian et al. [17] independently demonstrated the importance of optimizing process parameters, such as the feedstock temperature and injection pressure, to produce ceramic parts exhibiting high mechanical properties.

For the past fifteen years, the injection flow rate (also known as the injection speed) has been studied mainly in the context of the HPIM process. With the aid of numerical simulation, Atre et al. [18] observed that a high feedstock flow rate induced segregation caused by high shear rate gradient regions. Subsequently, Muangwaeng et al. [19] experimentally confirmed this segregation phenomenon induced by a high injection speed. SEM observations of their samples showed phase separation near the outer skin as well as black streaks near the gate (sign of thermal decomposition resulting from high friction) as the injection speed and pressure increased. Studying the influence of process parameters on the quality of MIM parts, Walcher et al. [20] showed that an increase in the injection speed led to a decrease in the surface roughness, along with an increase in the occurrence of parting lines. Huang and Hsu [21] demonstrated that dimensional stability was difficult to control for parts molded at high injection speed. The authors explained that the shear rate increase inevitably arising from an increase in the injection speed in turn leads to an increase in the shrinkage rate, which promotes the deformation of green parts. They also observed that a higher injection speed results in a higher green density and higher sintered properties, mainly caused by an increase in injection pressure forcing more powder into the mold cavity. During the injection optimization phase, Amin et al. [22] concluded, contradicting prior research results, that the effect of the injection flow rate on the green density was too low and could be neglected for their experiment. Askari and Momeni [23] recently demonstrated that the injection speed has a greater more impact on green properties than the other process parameters (injection temperature, mold temperature and holding pressure). They confirmed the results obtained by Huang and Hsu, in which an increase in the injection flow rate led to an increase in both the green density and in the flexural green strength. Using an X-ray tomography approach, Yang et al. [24] observed that an increase in the injection speed and pressure, which in fact inhibits the solidification of the feedstock during injection in the mold cavity, led to a decrease in the amount and size of porosities. They also confirmed that small cracks and large pores originating from the jetting phenomenon appeared, respectively, at too-low and too-high injection speeds. Using the LPIM process, Sardarian et al. [25] observed a low variation of the green density and flexural green strength for specimens injected at different velocities. However, a significant

change in these two metrics was observed at high temperature and high speed due to the presence of voids caused by jetting.

The influence of injection parameters on the overall quality of green parts is relatively well documented for high-viscosity feedstocks used in the HPIM process. However, to the best of the authors' knowledge, the impact of the injection speed on the injection pressure has never been studied for low-viscosity powder–binder mixtures used in the LPIM process. This work aims to quantify the influence of different injection parameters (including the injection flow rate) on the quality of green parts, based on the in-cavity pressure developed during the LPIM process, the visual aspect of the green parts, and local powder concentration.

2. Materials and Methods

2.1. Feedstock Formulation

A water-atomized 17-4 PH stainless-steel powder (Epson Atmix Corporation, Aomori, Japan) was mixed with a wax-based binder to formulate two feedstocks. A scanning electron microscope and a laser diffraction particle analyzer (LS 13320 XR, Beckman Coulter, Brea, CA, USA) (details provided in Table 1) were used to observe the particle shape and measure the particle size distribution reported in Figure 1. This MIM powder exhibits a near-spherical shape (Figure 1a) with a D_{10} , D_{50} , and D_{90} of about 3, 11, and 28 μm , respectively (Figure 1b). The powder was mixed with a blend of paraffin wax, carnauba wax, stearic acid, and ethylene-vinyl acetate in the proportion listed in Table 2. Two feedstocks (F60 and F65) were formulated at 60 and 65 vol. % of powder by changing the paraffin wax proportion. As seen in Figure 1c, the critical solid loading was determined at around 66 vol. % of powder, i.e., the value where the feedstock density starts to diverge from the theoretical line (black arrow in Figure 1c). Based on this result, the maximum solid loading was set to 1 vol. % below this threshold value, indicated by the white arrow in Figure 1c. Since a higher solid loading is generally required in MIM (i.e., for controlling shrinkage and final dimension during the sintering stage), the feedstock F65 corresponds to the maximum workable value for this specific powder. On the other hand, the feedstock F60 was arbitrarily selected as 5 vol. % below the maximum value (indicated by the grey arrow in Figure 1c). This low solid loading was specifically selected to study the influence of injection parameters on injection pressure using a mixture with properties quite different from the former, but also largely reported in the literature. The paraffin wax (PW) was used as the main constituent for its low viscosity, constant rheological properties, and low cost. The carnauba wax (CW), stearic acid (SA), and ethylene-vinyl acetate (EVA) were added to increase the green strength, to facilitate parts demolding, to promote the chemical bridge between the powder and binder, and to control the segregation and homogeneity of the feedstocks. A trial-and-error approach was used in our group [26] to experimentally determine that this proportion of each was the minimum value to promote the surfactant effect, reach a no-segregation condition, and to produce adequate green strength by adding SA, EVA, and CW, respectively. The balance of PW should be high enough for its fluidity property.

Table 1. Equipment used to characterize the dry powder.

Equipment	Supplier	Model	Mode	Detail
Scanning electron microscope	Hitachi, Tokyo, Japan	3600	Secondary electrons detector	20 kV; working distance of 15 mm; powder deposited on a carbon tape
Particle analyzer	Beckman Coulter	LS 13320 XR	Dry powder module	Fraunhofer theory with an 8% obscuration target.

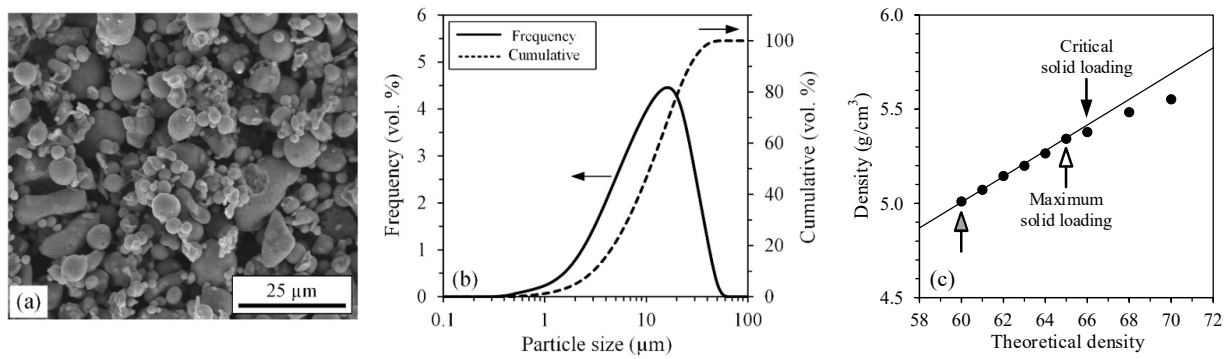


Figure 1. (a) SEM observation; (b) particle size distribution of the 17-4 PH powder.

Table 2. Volume fraction of the powder and polymeric constituents used for feedstock formulations.

Feedstock	Vol. %				
	Powder	Paraffin Wax	Carnauba Wax	Stearic Acid	Ethylene-Vinyl Acetate
F60	60	30	7	2	1
F65	65	25	7	2	1

2.2. Feedstock Characterization

The density of the powder, of the single binder constituents, and of the feedstock was measured using a helium gas pycnometer (AccuPyc II 1340) according to the ASTM B923 standard [27]. The melting point of each binder constituent was measured using a differential scanning calorimeter (Perkin Elmer Pyris 1 DSC) according to the ASTM D3418 standard [28]. The physical properties of each feedstock constituent are presented in Table 3. The feedstock viscosity presented in Figure 2a was measured at three different temperatures (80, 90, and 100 °C) and different shear rates (0.5 to 3500 s⁻¹) using a rotational rheometer (Anton Paar, MCR 302) equipped with a concentric cylinder cell (CC-17) and a Peltier temperature-controlled measuring system (C-PTD 200). The properties for the feedstock F60 were obtained in [26], while the properties of the feedstock F65 were obtained in the framework of the present work. The shear thinning behavior of the feedstocks as well as the influence of temperature on viscosity was captured using the second-order viscosity model as follows:

$$\ln\eta = A + B\ln\dot{\gamma} + CT_c + D(\ln\dot{\gamma})^2 + E\ln\dot{\gamma} + FT_c^2 \quad (1)$$

where η is the feedstock melt viscosity, $\dot{\gamma}$ is the shear deformation rate, T_c is the corresponding relative temperature in Celsius, and A , B , C , D , E , and F are data-fitted coefficients of the second-order model, reported in Table 4. The viscosity curves were fitted using Equation (1) and the resulting curves are superimposed in Figure 2a for each test condition. The DSC thermograms presented in Figure 2b were used to determine the feedstocks' transition temperature (extracted from the cooling stage as identified by black arrows) and specific heat (C_p) according to the standard test method ASTM-E1269 [29], as presented in Figure 2c. The thermal conductivity (k) of the feedstocks reported in Figure 2d was measured according to the transient line-source technique described in the standard test method ASTM- D5930 [30].

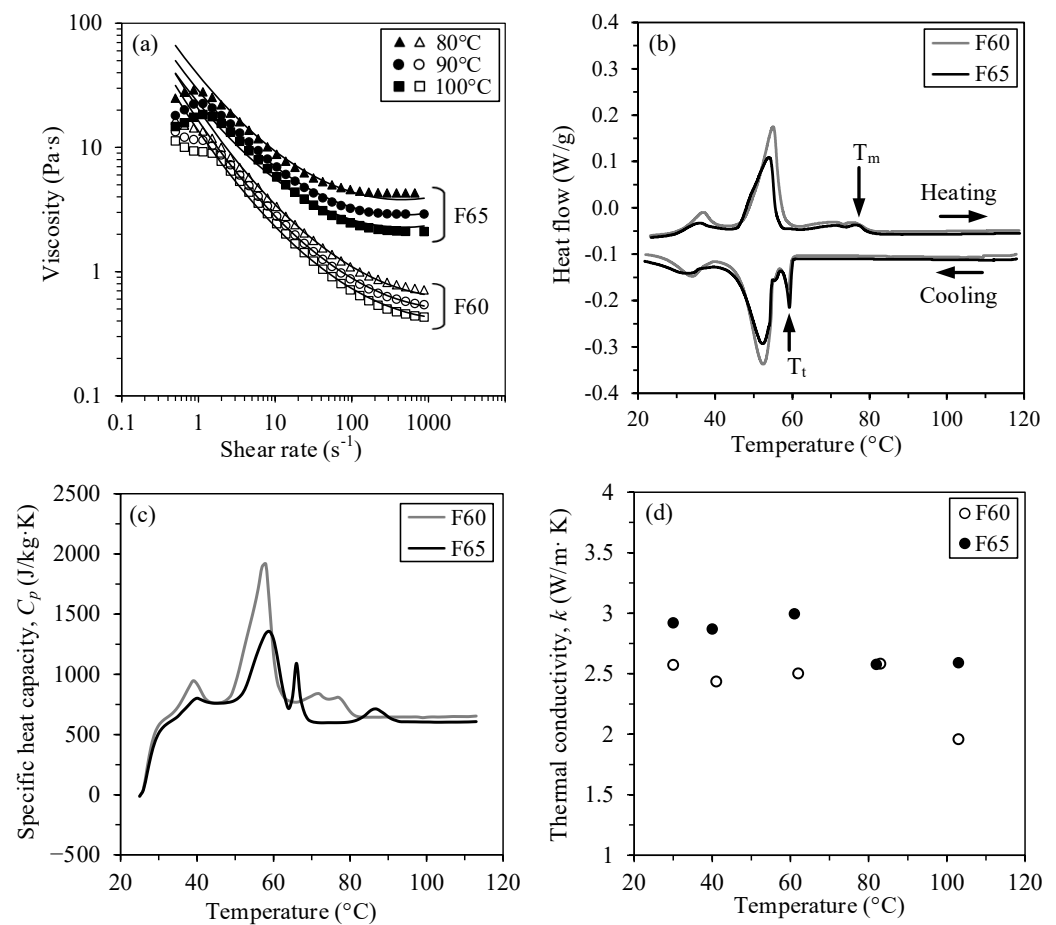


Figure 2. Rheological and thermal properties of feedstocks F60 and F65: (a) viscosity profiles, (b) DSC thermograms, (c) specific heat, and (d) thermal conductivity measured at different temperatures.

Table 3. Physical properties of the constituents used for feedstock formulation (data obtained in [26]).

Constituents	Melting Point (°C)	Density (g/cm ³)	Supplier
17-4PH powder	>1404	7.69	Epson Atmix Corp.
Paraffin wax	59.0	0.90	Sigma-Aldrich, St. Louis, MO, USA
Carnauba wax	84.5	1.00	Sigma-Aldrich
Stearic acid	75.0	0.90	Sigma-Aldrich
Ethylene vinyl acetate	49.0	0.98	Dupont, Wilmington, DE, USA

Table 4. Second-order data-fitted coefficients for feedstocks F60 and F65.

Fitted Coefficient	F60	F65
A	5.574	7.819
B	-3.987×10^{-1}	-5.569×10^{-1}
C	-4.136×10^{-2}	-7.336×10^{-2}
D	5.850×10^{-2}	6.149×10^{-2}
E	-5.047×10^{-1}	-1.967×10^{-1}
F	1.169×10^{-4}	2.645×10^{-4}

2.3. Real-Scale Injection

Real-scale injections were performed using a laboratory injection press schematized in Figure 3a, which is the new version of the injection principle developed by Lamarre et al. [31,32]. Powder and binder were mixed at 90 °C using a planetary blender under vacuum to produce homogeneous and bubble-free molten feedstock. The prepared feedstock was

directly pulled from the mixing system by the action of a heated cylinder/piston system acting as a syringe (Figure 3b). The filled cylinder attached to the injection table was slid before being aligned and clamped with the mold (Figure 3c), and the feedstock was injected into the mold cavity at a constant flow rate (Figure 3d). After the feedstock was completely solidified, the clamping pressure was released, the mold removed (Figure 3e), and the sliding platform moved back and aligned with the mixing system (Figure 3f) before the remaining molten feedstock was pushed back inside the container for the next injection (Figure 3g). The simple rectangular mold geometry ($3.1 \times 25.4 \times 164$ mm) presented in Figure 3h was used to quantify the effect of injection process parameters on the in-cavity pressure. This mold was instrumented with a piezoresistive pressure sensor (Keller Y25 series: 0–100 kPa \pm 0.5 kPa for low pressure and 0–1000 kPa \pm 2.5 kPa for high-pressure) positioned above the gate, while the mold temperature was monitored by a thermocouple located inside and close to the cavity. Data were recorded by an acquisition card (NI USB-6212) using LabVIEW. The complex shape part presented in Figure 3i was finally used to demonstrate the ability of the LPIM process to produce intricate parts with different features, such as threaded holes, small holes, and complex contoured surfaces.

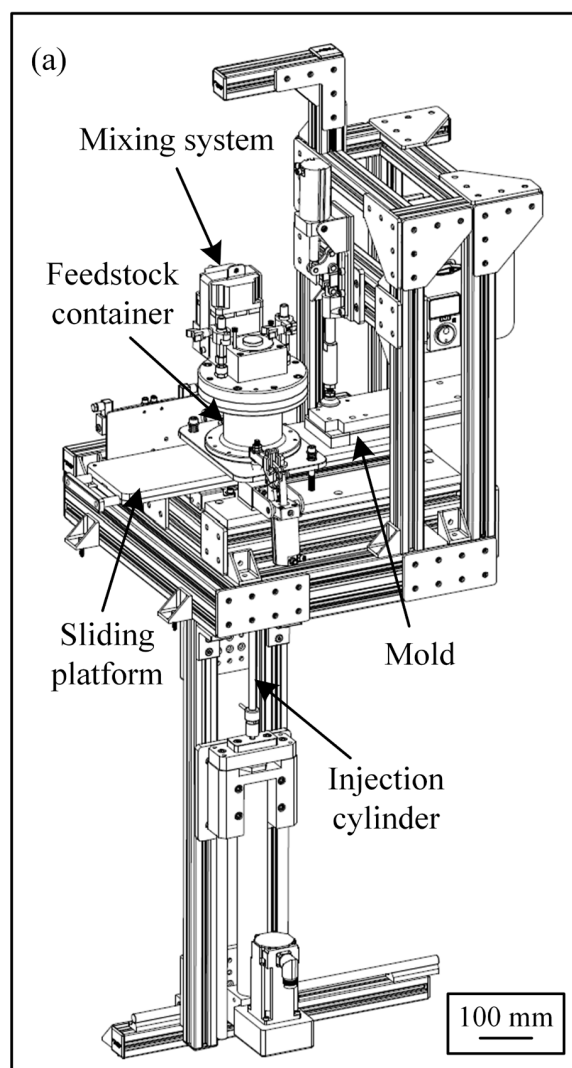


Figure 3. Cont.

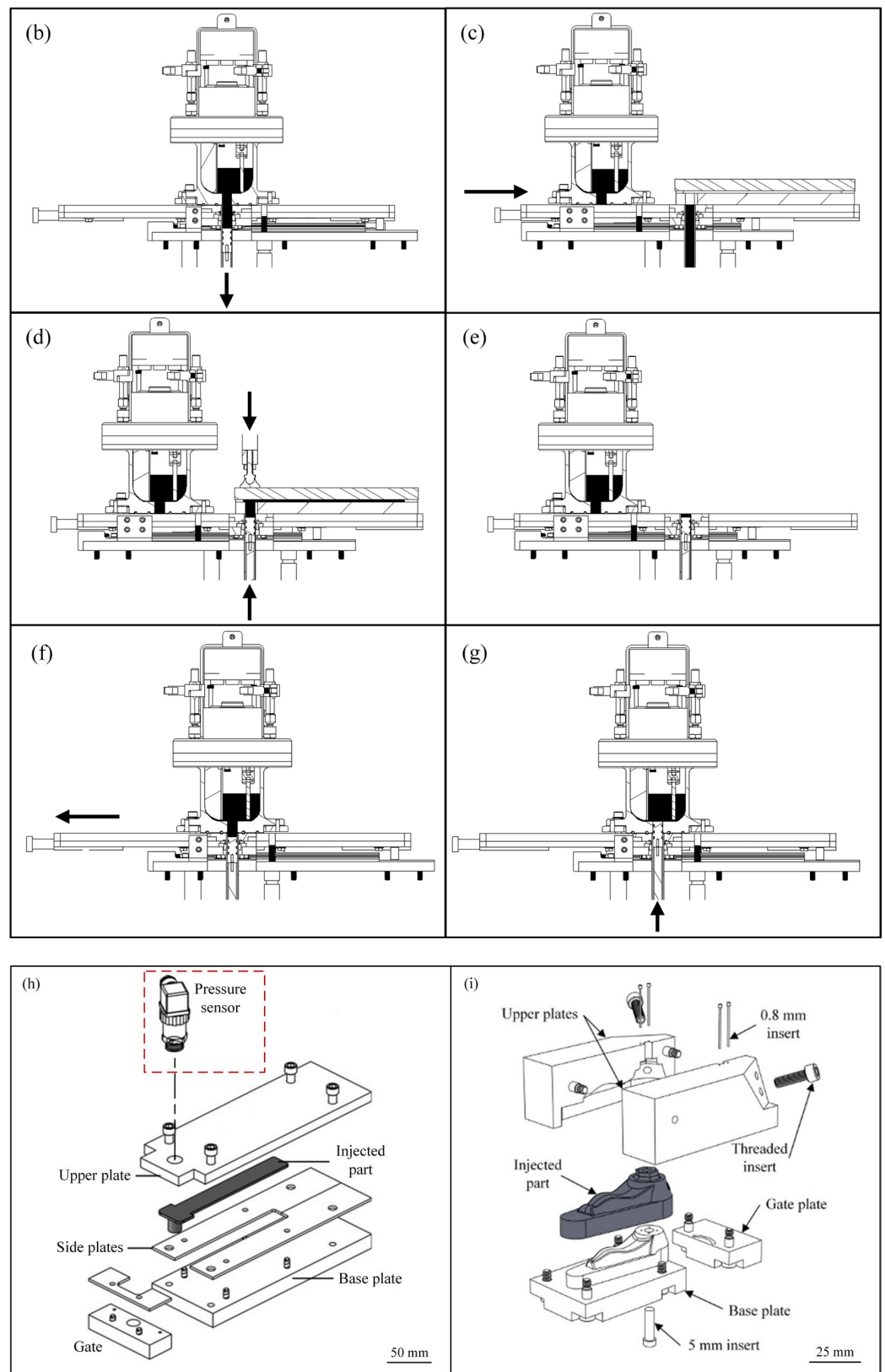


Figure 3. (a) General view of the injection system in mixing position, (b–g) partial cross-section views of the injection system detailing the injection sequence, (h) rectangular mold, and (i) complex shape mold (black arrows represent the movement of the piston and the table).

The process parameters for the real-scale injections and numerical simulations are reported in Table 5 for each injection sequence. These process parameters were grouped into

four sequences to capture the influence of the mold temperature, feedstock temperature, and injection flow rate on the injection pressure, visual aspects, and segregation. During sequence #1, the pressure was experimentally determined using the rectangular mold maintained at a temperature of 30, 40, and 50 °C (other conditions were kept constant). During sequence #2, a similar approach was used by changing the feedstock temperature from 80 to 100 °C and keeping the mold temperature constant at 40 °C. During sequences #3–4, an injection flow rate ranging from 1 to 30 cm³/s was used with the two molds presented in Figure 3h,i to obtain the injection pressure and flow behavior, while keeping the mold and feedstock temperatures constant at 40 and 90 °C, respectively. The mold and feedstock temperature ranges represent typical values for wax-based feedstocks, while the minimum and maximum flow rates (i.e., 1 and 30 cm³/s) correspond to the minimum and maximum injection speeds (i.e., 0.5 and 15 cm/s of the linear piston) possible with the laboratory injection press described above. Note that the molds were not equipped with heating/cooling channels to control the surface cavity temperature during the injections. Therefore, the mold temperature corresponds to the initial temperature of the mold before injections.

Table 5. Process parameters used for numerical simulations and real-scale injections.

Sequence	Mold Temperature (°C)	Feedstock Temperature (°C)	Flow Rate (cm ³ /s)	Solid Loading (vol. %)	Mold Type
1	30	90	15	60/65	Rectangular
	40				
	50				
2	40	80	15	60/65	Rectangular
		90			
		100			
3	40	90	1	60/65	Rectangular
			2		
			3		
			5		
			7		
			10		
			15		
20					
30					
4	40	90	1	60/65	Complex shape
			5		
			30		

2.4. Numerical Simulations

The influence of the injection parameters on mold in-cavity pressure was also numerically simulated using Moldflow Insight 2019 (Autodesk Inc., San Francisco, CA, USA). The powder injection molding (PIM) module and the filling analysis sequence were selected as they allow the prediction of the powder concentration variation during the filling phase of the injection. The physical, rheological, and thermal properties, as well as the solid loading presented in Figure 2, were implemented as material properties. The melt-to-solid transition temperature of the two feedstocks was set at 62 °C, which corresponds to the transition temperature of the paraffin wax highlighted in Figure 2b. The value of the heat transfer coefficient (HTC) between the mold and the feedstock was set at 100 kW/(m²·°C) according to previous works carried out by Ilinca et al. [33]. This coefficient accounts for any heat transfer resistance at the cavity's surface. Accelerating and decelerating speed ramps were used to replicate the experimental injection speeds. The CAD models of the two parts were both meshed using 3D tetrahedral elements with an edge length of 0.5 mm. The rectangular and complex geometries illustrated in Figure 4a,b were meshed using 1.8 and 2.4 million of elements, respectively. The overall dimensions of these two parts are shown in Figure 4c,d. The pressure obtained numerically was extracted from the nodes included

in the corresponding area in contact with the experimental sensor ($\varnothing 17$ mm located at the top of the gate, see Figure 3h) and averaged using a Python script developed.

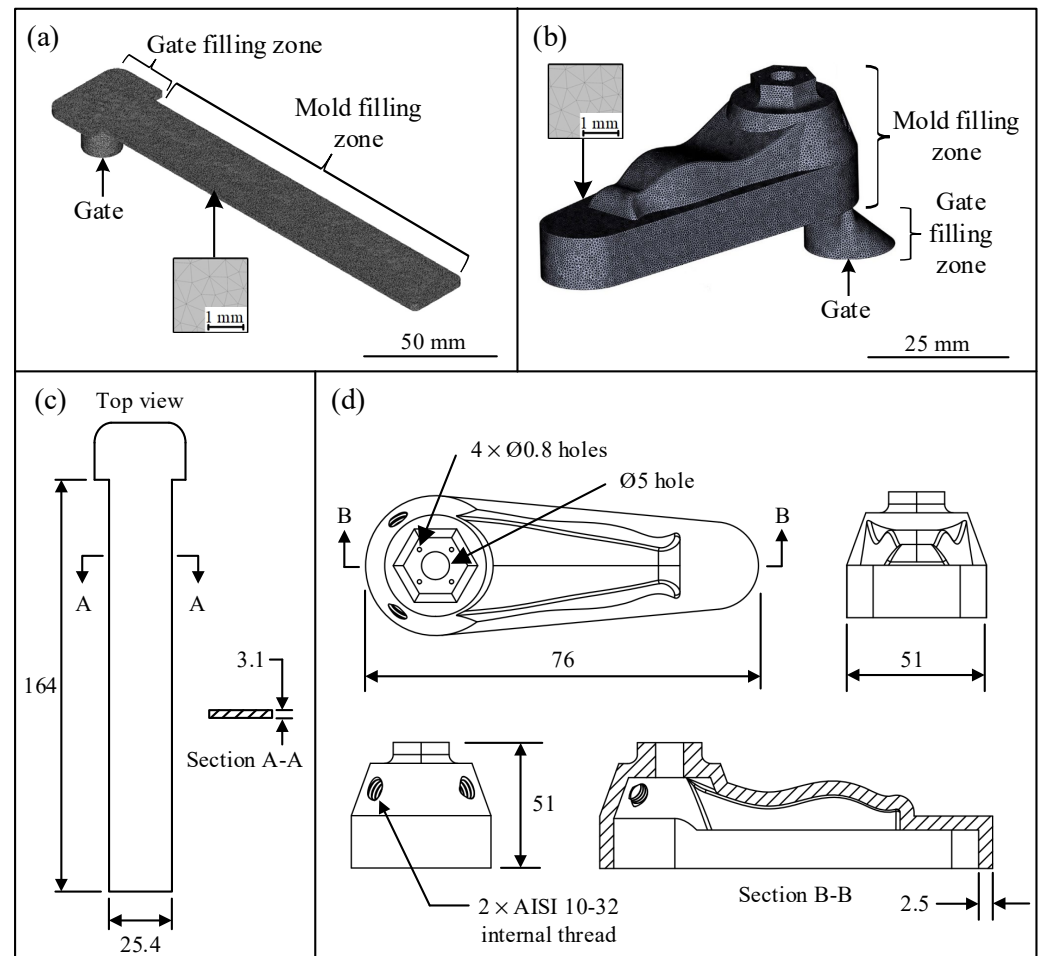


Figure 4. Representation of the (a) rectangular part, and (b) complex shape part with the superimposed finite element meshing.

2.5. Powder Segregation Measurements

Powder segregation was characterized using a PerkinElmer STA8000 thermogravimetric analyzer (TGA) (PerkinElmer, Waltham, Massachusetts, USA) according to the method developed in a previous study [34]. Segregation, also known as inhomogeneous powder distribution over an injected part, was investigated because the phenomenon may lead to distortions, cracks, voids, warping, and heterogeneous shrinkage during sintering. Segregation usually results from an improper mixing method during feedstock preparation, from gravity when the feedstock is idle during process dead times, or from the presence of high shear deformation rate gradients during the molding process. Specimens measuring about 1 mm^3 were extracted from each part injected during sequence #4 presented in Table 5 according to the position locations A to E presented in Figure 5a. The specimens were placed in a standard ceramic pan and then heated from 30 to 550 °C at a heating rate of 20 °C/min under nitrogen purge gas, with a flow rate of 60 mL/min. The weight fraction of the remaining powder after binder burnout was determined from the TGA profiles, as illustrated in Figure 5b, and converted in terms of volume fraction of powder according to Equation (2).

$$\text{vol. \% powder} = \left[1 + \left(\frac{\rho_{\text{powder}}}{\rho_{\text{binder}}} \right) \cdot \left(\frac{1}{\text{wt. \% powder}} - 1 \right) \right]^{-1} \quad (2)$$

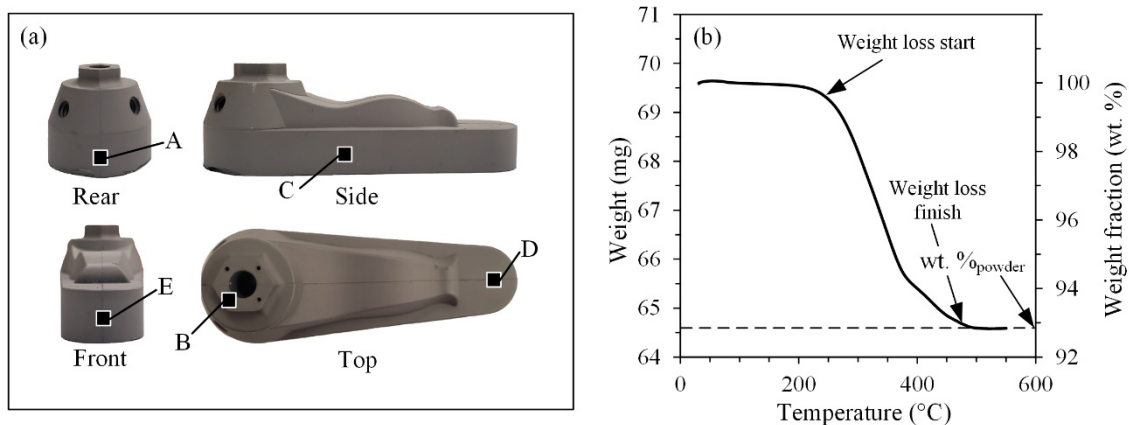


Figure 5. (a) Rear, side, front, and top views of a typical complex shape green part showing the positions (A to E) of the extracted specimens for TGA tests, and (b) typical TGA curve used for quantification of powder concentration within an injected specimen.

3. Results and Discussion

3.1. Influence of the Mold and Feedstock Temperature on Injection Pressure

Figure 6 presents the pressure profiles measured in the rectangular mold cavity at different mold temperatures (sequence #1 in Table 5) and feedstock temperatures (sequence #2 in Table 5) for feedstocks F60 and F65. These profiles were calculated from three tests, and the maximum standard deviations of these measurements were low (± 3 and ± 10 kPa for the low- and high-pressure sensors, respectively) and are not represented in these figures for better clarity. The pressure profiles are divided into two zones: the gate-filling zone (vertical cylinder and its adjacent wide rectangular section) and the mold-filling zone (constant width rectangular cavity), both described in Figure 3h. The pressure value recorded during the gate-filling zone remains at zero since the sensor (located at the top of the gate) is not in contact with the molten feedstock during this phase. As the feedstock converges through the mold-filling zone illustrated in Figure 4a, the feedstock is confined within the gate zone and, thus, comes in contact with the pressure sensor to record the evolution of pressure according to the filling stage.

For a given mold temperature (Figure 6a,b) or feedstock temperature (Figure 6c,d), the pressure in the mold cavity increases almost linearly as the filling stage becomes longer to overcome the higher friction, i.e., higher mold contact surface against the feedstock flow. During these injections performed at a constant volumetric flow rate, an increase in a mold or feedstock temperature results in a decrease in injection pressure for both feedstocks. This expected trend is certainly due to the decrease in feedstock viscosity observed in Figure 2a, when the mixture is hotter, because it cools down more slowly. Indeed, a decrease in the feedstock temperature from 100 to 80 °C produces an increase in its viscosity, respectively, from 0.5 to 0.8 Pa·s or 2 to 4.1 Pa·s for feedstocks F60 and F65 (values extracted in a typical shear rate at 100 and 500 s^{-1} in Figure 2a). These relative increases of about 160% and 205% in feedstock viscosity are proportionally correlated with the additional pressure required to inject the feedstocks at 100 and 80 °C. Similarly, the viscosity difference of about 5–7 times also roughly correlates with the pressure difference required for the two feedstocks F60 and F65.

With a relative difference varying from 0 to 35%, the injection pressures predicted by the numerical model were relatively close to those obtained experimentally. This first validation phase confirmed that the input parameters are appropriate for assessing the magnitude of the pressure experienced by the feedstock in the mold. Interestingly, the pressure values predicted in the extreme condition of the thermal transfer between the feedstock and the mold were in very good agreement with the experimental observations, with relative differences below 10%. This extreme condition consists of promoting the solidification by decreasing the mold or feedstock temperature. In Figure 6a–d, this state can

be obtained (or tended to be attained) with the mold at 30 °C and the feedstock at 80 °C. The more accurate results obtained in this state could be explained by the fact that this specific experimental injection was performed more in line with the thermal transfer conditions implemented in the numerical model. Indeed, in the current version of Moldflow Insight 2019, the PIM module uses a constant wall temperature, and the rest of the mold shell is able to keep this temperature low and constant, as seen in a conventional HPIM. However, and as used in the present work, LPIM molds are rarely provided with conformal cooling channels, exhibiting a high capacity to quickly extract large amounts of heat. Therefore, the increase in the relative differentials between simulations and experiments as the mold or feedstock temperature increase can simply be explained by the fact that the experimental setup includes more of a slow and natural thermal transfer approach that is not taken into account by the model. In line with this assumption, the feedstock formulated at a higher solid loading exhibits a lower relative difference between experimental and numerical pressures, probably due to its higher thermal conductivity.

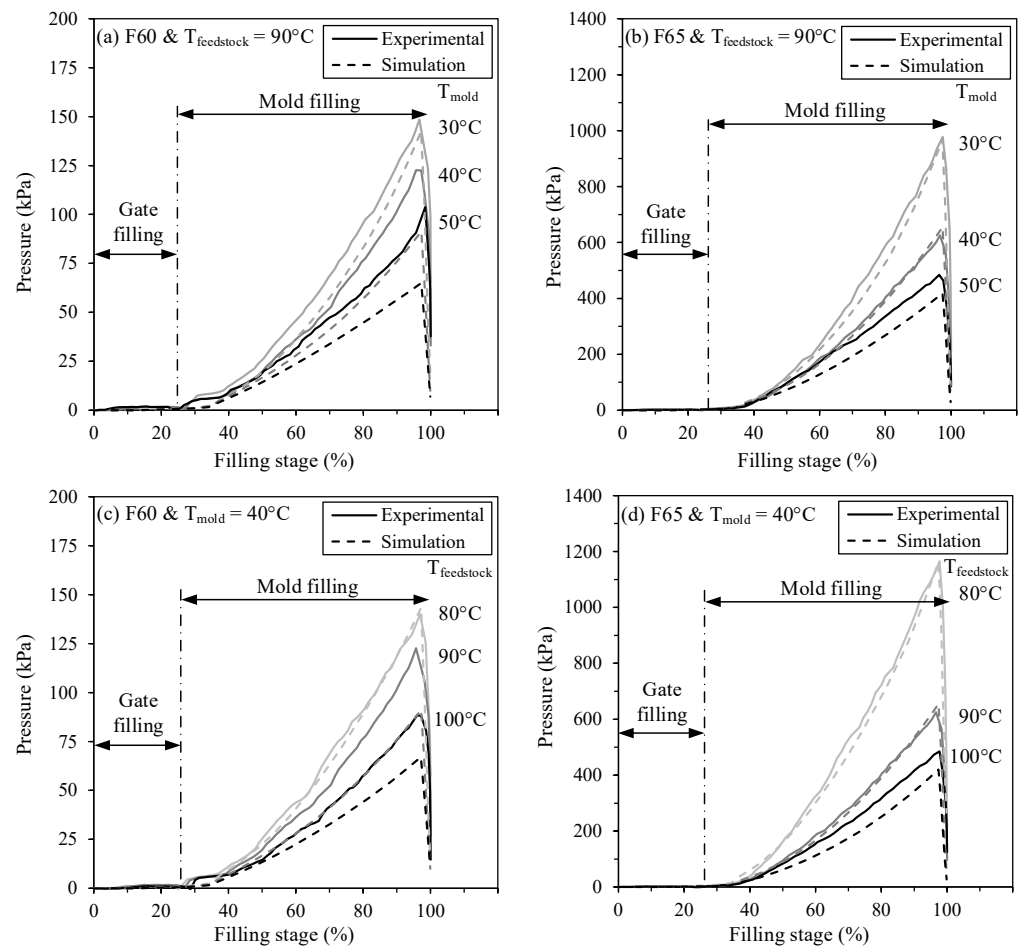


Figure 6. Influence of mold (a,b) and feedstock temperatures (c,d) on experimental and numerical in-cavity pressure for the feedstocks F60 and F65 (constant flow rate of 15 cm³/s). Different color lines represent different mold and feedstock temperatures.

To reinforce this hypothesis, additional injections were performed to promote the solidification extreme condition discussed above, as well as to test a second but opposite extreme condition. On the one hand, experimental and numerical pressure values were obtained in Figure 7a in a quasi-adiabatic condition by injecting a feedstock at 90 °C into a mold at 80 °C to minimize significant heat transfer at the mold/feedstock interface and avoid fast solidification during injection. On the other hand, an experimental mimic of the thermal transfer simulated by Moldflow was performed by decreasing the mold temperature to

25 °C and the feedstock temperature to 75 °C and is presented in Figure 7b. Although the temperature difference between the feedstock and the mold of this latter extreme condition is higher than one condition used above in Figure 6b, these low temperatures forced feedstock to solidify rapidly on the mold surface, since it is close to its melting point. Note that these latter conditions represent the lowest temperatures that can be practically used at a high injection flow rate in this project to avoid early solidification. Using this extreme condition, the experimental pressure measured with the feedstock F65 exhibits a constant pressure stabilized around 2200 kPa from a filling stage of about 85%. This plateau appears because the sensor has simply reached its true maximum capacity (i.e., from a rule of thumb: $1000 \text{ kPa} \times \sim 2$) and can therefore no longer return a pressure measurement. Except for this plateau for feedstock F65, the similar results between experiments and simulations for these two extreme thermal transfer conditions presented in Figure 7 confirm that experiments that are not performed close to these conditions cannot be used to accurately validate the simulations. In other words, the slow and typical thermal transfer conditions occurring in LPIM seem to significantly drive the in-cavity pressure, which is, in fact, not properly captured by the numerical model.

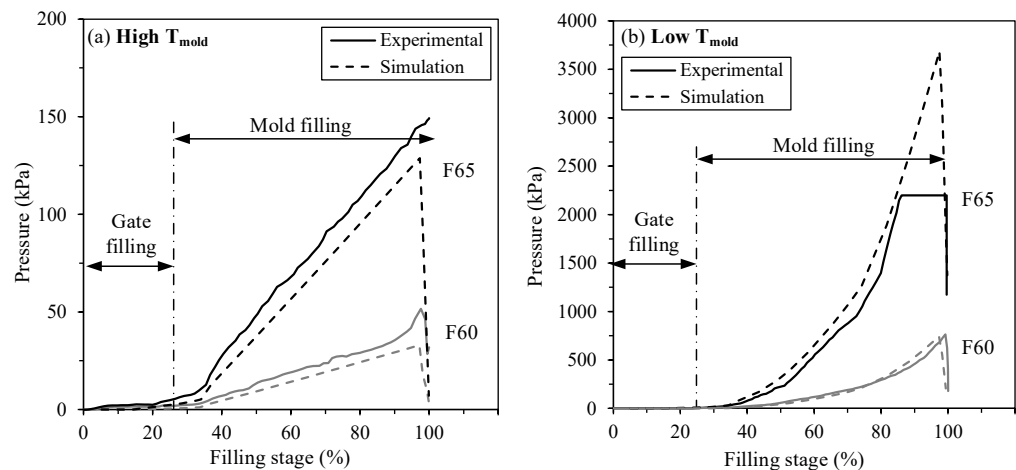


Figure 7. Extreme injection conditions (high and low T_{mold}) obtained experimentally and numerically. Different color lines represent different feedstocks.

3.2. Influence of Injection Flow Rate on Pressure

Figure 8 presents the evolution of the in-cavity pressure obtained experimentally and numerically at different injection flow rates (sequence #3 in Table 5). To that end, pressure values were extracted from pressure profiles at a mold-filling stage of 85% (real-scale or simulated injections profiles similar to those presented in Figure 6). In addition to confirming the impact of solid loading on the injection pressure, these curves present an unexpected trend, which can be divided into two distinctive segments, identified as segments “I” and “II” in Figure 8. In segment I, the injection pressure obtained experimentally as well as numerically decreases as the flow rate increases, regardless of the powder volume fraction. Visual inspections on parts fabricated with these low injection flow rates confirm that this high cavity pressure originates from early feedstock solidification or partial solidification, which may lead to an increase in the feedstock viscosity, as well as in friction with the mold walls (note that the visual inspection of parts is addressed below in this work). An increase in the flow rate naturally decreases the total injection time, which reduces the volume of feedstock susceptible to solidification during the injection process and, finally, reduces the overall injection pressures.

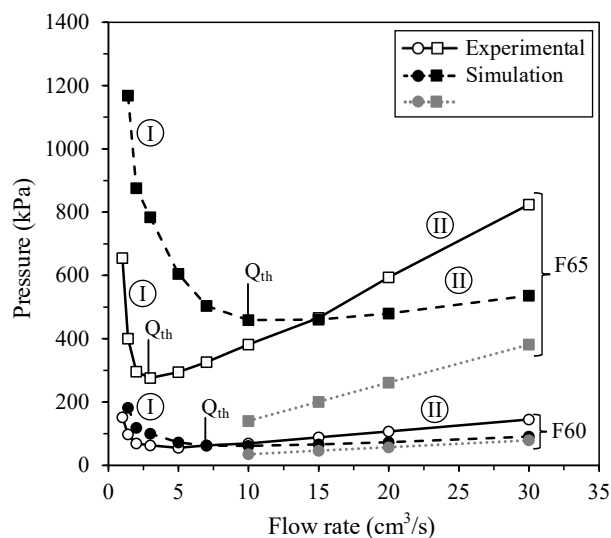


Figure 8. Comparison of experimental and simulated in-cavity pressures obtained at different injection flow rates (values extracted from the pressure profiles at a mold-filling stage of 85%). “I” and “II” represent the two distinctive segments of the curves.

At a certain flow rate threshold (identified as Q_{th} in Figure 8), the slope of each curve changes to exhibit a proportional increase in the pressure with the flow rate (identified as segment II in Figure 8). Such a linear trend can be also anticipated by Poiseuille’s law $P = \frac{12Q\eta L}{wt^3}$ [35], taking into account the volumetric flow Q , the cross-section dimensions of the mold w and t , and the length of the mold cavity L . The feedstock viscosity η was extracted from Figure 2a at the shear rate experienced by the feedstock over the flow front. These values represent an average shear rate of 125, 200, 250, and 400 s^{-1} for the feedstock F60, and 100, 150, 200, and 350 s^{-1} for the feedstock F65 obtained for 10, 15, 20, and $30 \text{ cm}^3/\text{s}$, respectively. Considering that all applicability conditions for such an analytic model are not gathered (e.g., Newtonian fluid), this latter equation was only used to confirm the trend and the order of magnitude for the anticipated pressure obtained for the two feedstocks. For feedstock F60, the Q_{th} occurs with around the same flow rate of $7 \text{ cm}^3/\text{s}$, and the predictions obtained by the numerical simulations as well as those calculated by Poiseuille’s law are in good agreement with experimental pressures. On the left-hand side of the Q_{th} value, the model slightly overestimates the in-cavity pressure, while the opposite trend is seen on the right-hand side of the curve, where the simulations underestimate the experimental values. For feedstock F65, the same over- and underestimation trend is clearly visible. However, the curves exhibit significant discrepancies, particularly at low and high injection flow rates. Interestingly, the different Q_{th} values obtained experimentally ($Q_{th} = 3 \text{ cm}^3/\text{s}$) and numerically ($Q_{th} = 10 \text{ cm}^3/\text{s}$) reinforced the assumption that the numerical model does not take into account a few parameters particularly linked with the thermal transfer conditions seen in the LPIM process. Indeed, low flow rates (e.g., $2 \text{ cm}^3/\text{s}$) may produce injection times as long as 15 s that may heat the mold and experimentally maintain the feedstock viscosity lower than the value used in the simulations for this specific rectangular geometry. This variation of the mold temperature was experimentally recorded in Figure 9 by replacing the pressure sensor with a thermocouple holder used to introduce a thermocouple at 1 mm above the feedstock/mold interface (no measurement repetition was performed). At the end of the injection stage, an increase of about $8\text{--}9 \text{ }^\circ\text{C}$ was measured for a low flow rate of $2 \text{ cm}^3/\text{s}$, but an interface heating of only $2\text{--}3 \text{ }^\circ\text{C}$ occurring later in the process was reported for higher injection flow rates comprising between 15 and $30 \text{ cm}^3/\text{s}$. During the same injection performed at a low flow rate (Figure 8), the numerical model imposed a significantly lower feedstock/mold interface temperature (i.e., $T_{\text{mold}} = 40 \text{ }^\circ\text{C}$), which necessarily decreased the feedstock viscosity; this action created a frozen layer, or even partially solidified the feedstock, contributing to an overestimation

of the pressure values in segment I of the simulated curve. For feedstock F65, the slopes of segment II obtained experimentally and numerically were also significantly different. During experiments, a change from 5 to 30 cm³/s almost tripled the pressure required for the injections. This trend, which is also clearly anticipated by Poiseuille's law, was not captured by the simulation model, where an increase from 10 to 30 cm³/s had only a minor impact on the injection pressure. This difference in trends between the curves means that the simulated pressure is underestimated after the intersection point is exceeded, which is similar to what is observed for feedstock F60 at high flow rates. In addition to the thermal transfer conditions highlighted above, the results suggest that other experimental conditions, such as the mold surface finish, slight mold dimension variations, or minor temperature changes, were not considered by the numerical model. The influence of the flow rate on the injection pressure of low-viscosity feedstocks, quantified experimentally for the first time in the framework of this study, thus continues to be a challenge when it comes to numerical simulation, since the LPIM conditions (far from those used in conventional HPIM) do not appear to be adequately implemented in the numerical model. Although the overall pressure magnitude was fairly well predicted by the simulations, future works are needed to adapt the numerical model to the specific thermal and physical conditions seen in the LPIM process. In other words, this work confirms that the interface temperature between the feedstock and the mold in LPIM probably cannot be maintained at a constant value, as experienced in the HPIM process.

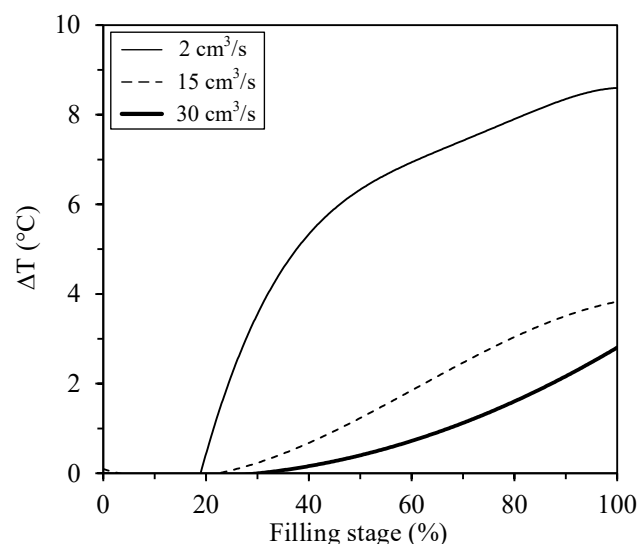


Figure 9. Mold temperature variation during injection.

3.3. Influence of Injection Flow Rate on Green Part Quality

In this work, the part quality was assessed by visual inspections and quantifications of the occurrence of segregation. The complex shape parts presented in Figure 10 were injected with the two feedstocks, using three different flow rates. At a low injection flow rate of 1 cm³/s, several visual defects were revealed at the surface of the parts, as indicated by the black arrows in Figure 10a,b. At a low solid loading (feedstock F60), weld lines and flow marks were observed scattered at the top and side of the injected parts. Similar defects were visible on the parts injected with the high solid loading feedstock (feedstock F65), in addition to clear cracks, incomplete filling, and sinks. As noted above, a too-low injection flow rate seems to produce early feedstock solidification, which occurs in the presence of an increase in the powder volume fraction thanks to its higher thermal conductivity. Repeated injections under these conditions confirm that these defects are always present but can be localized in different places within the part. At a moderate flow rate of 5 cm³/s, no visual surface defect was seen for the two feedstocks in Figure 10c,d. The parts were smooth, and features such as small holes, thin walls, and threaded holes were well defined. Since this

mold was opened laterally (see Figure 3i), only a small and continuous flashing, indicated by a white arrow, was visible along the parting line of parts injected under this condition. At a high flow rate of $30 \text{ cm}^3/\text{s}$, the presence of external defects depends on the solid loading. Feedstock F60 produced the same part quality as the one obtained at a moderate flow rate (Figure 10e), but surprisingly, for feedstock F65, cracks were observed in the front area of the injected part (indicated by grey arrows in Figure 10f). Such unexpected defects may be caused by residual stress, or any local intricate pressure/shear rate pattern induced by the higher mold pressure required for this specific feedstock at high injection flow rates (see Figure 8). The numerical model was used to visualize the flow of the feedstock in the mold cavity (Figure 8h), as well as assess the injection pressure at the end of filling this complex shape part in Figure 8g. After the first second, almost 50% of the mold cavity volume is filled where the two feedstock fronts meet at the center along the parting line. Just before the mold is completely filled, the pressure measured at various points in the part confirms that a low pressure ranging from 2 to 270 kPa is required for this kind of thin complex shape part.

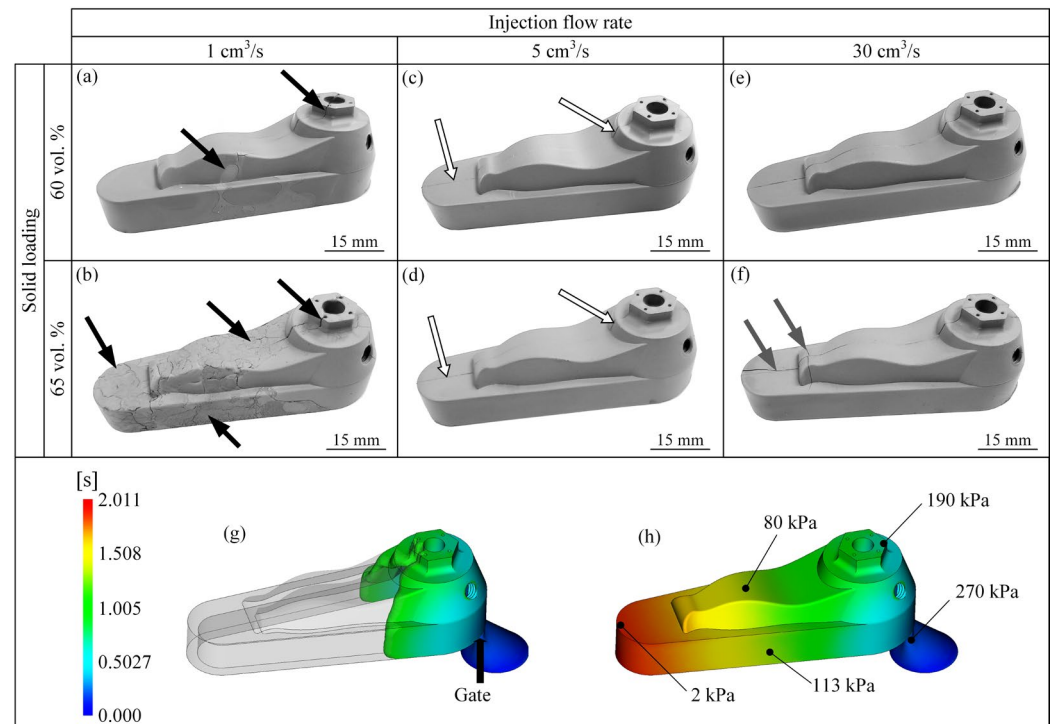


Figure 10. (a–f) Typical injection results showing the influence of the feedstocks and flow rates on visual part quality; (g,h) numerical result of the flow and pressure within the part calculated for a flow rate of $15 \text{ cm}^3/\text{s}$.

Figure 11 reports the local volume fraction of powder measured at different locations of the complex shape part presented in Figure 5. The solid lines represent the nominal solid loading of feedstocks F60 and F65, while the dashed lines denote the sensitivity limit of the TGA technique when it comes to detecting a real change in local solid loading. This detection range of $\pm 0.25 \text{ vol. } \%$ of powder was defined in our previous work [34] and confirmed by [36]. The results obtained for feedstock F60 (Figure 11a) are within or just slightly outside the detection limit of the measurement technique. This confirms that the injection flow rate has almost no effect on variations of the powder volume fraction for this feedstock, except on the side of the part (specimen location C) injected at $1 \text{ cm}^3/\text{s}$. This local increase of about 2.6 vol. % of powder could be caused by the early solidification clearly visible in Figure 10a, which may produce a nonuniform filling, leading to unexpected/intricate shear rate gradients, which drag more powder into this zone.

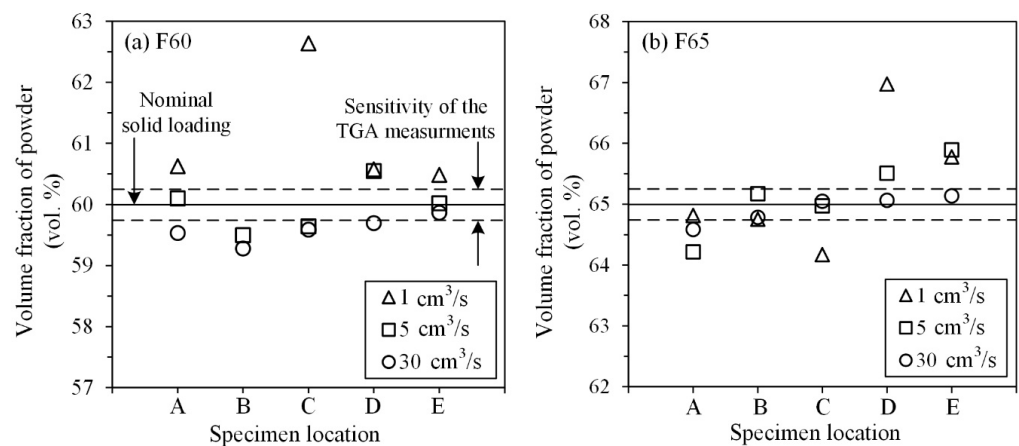


Figure 11. Powder volume fraction (vol. %) measured at different specimen locations on complex shape parts injected at flow rate using the feedstocks (a) F60 and (b) F65.

For feedstock F65 (Figure 11b), the powder volume fraction seems to be slightly lower near the gate (specimen location A) and slightly higher at the front of the part (specimen location E). This can be explained by the higher pressure required to inject such high solid loading feedstock (Figure 8) combined with an abrupt change in the injection channel within this gate/part region that was identified as a potential powder–binder separation zone by Thornagel et al. [37]. In this respect, the binder-rich zone created in the gate may finally lead to a powder-rich zone uniformly transported up the front of the injected part, i.e., the last region to be filled by the molten feedstock. Similarly to the previous feedstock, a too-low flow rate of 1 cm³/s produces premature solidification zones, as shown in Figure 10b by weld lines and cracks; these zones may also contribute to locally changing the shear rate gradient, leading to the significant segregation seen on the side (specimen location C) and the front of the part (specimen locations D–E). At high solid loading and high injection flow rates, no real segregation was measured.

4. Conclusions

A laboratory injection press was developed and used to measure the mold in-cavity pressure during the low-pressure powder injection molding process (LPIM). An experimental characterization and real-scale injections were performed with two feedstocks formulated from a water-atomized 17-4PH stainless-steel powder mixed with a wax-based binder system at a solid loading of 60 and 65 vol. % of powder. The feedstock properties, such as the viscosity, melting point, transition temperature, thermal conductivity, density, and specific heat capacity, were experimentally characterized and implemented as material properties in a Moldflow numerical model. The numerically obtained injection pressures were compared with experimental results using different injection parameters, such as the mold temperature, the feedstock temperature, and the injection flow rate. The influence of injection flow rates on green component quality and local segregation was experimentally studied. The investigation allowed us to reach a few conclusions, which are summarized as follows:

- An increase in mold temperature and feedstock temperature and/or a decrease in powder volume fraction produced a significant decrease in the in-cavity pressure, pointing to a strong correlation with the feedstock viscosity.
- The unexpected decrease in injection pressure observed during an increase in flow rate from 1 cm³/s to a flow rate threshold, Q_{th} (7 and 3 cm³/s for the 60 and 65 vol. % of powder feedstocks, respectively), was in fact due to early solidification of the feedstock and not feedstock flow behavior. Using injection flow rates $> Q_{th}$, the expected linear relationship between the pressure and feedstock flow was observed.

- The presence of visual defects was significantly reduced for injections at moderate flow rates, but an absence of the segregation phenomenon throughout green parts was seen when using high injection flow rates.
- The simulation model was able to capture the injection pressure only when the injection flow rate was kept constant or when thermal transfer conditions were extreme (where solidification was promoted or avoided by decreasing or increasing the mold temperature). This suggests that the thermal behavior observed in the LPIM process (which is significantly different from the one seen in conventional HPIM) could not properly be taken into account in the model. Since this work represents, to the best of the authors' knowledge, the first experimental validation of the simulated pressure in LPIM, future works addressing this issue are thus needed to accurately predict the numerical mold cavity pressure for LPIM feedstocks when different injection flow rates are used. To that end, a thermal law (instead of a constant temperature value experienced in HPIM) should be implemented in Moldflow to take into account the mold heating typically seen in the LPIM.

Author Contributions: F.A.: Methodology, numerical simulations, validation, writing—original draft, visualization. D.D.: Methodology, writing—original draft, visualization. V.D.: Supervision, conceptualization, project administration, writing—review and editing. All authors have read and agreed to the published version of the manuscript.

Funding: This work was carried out with the financial support of the Natural Science and Engineering Research Council (NSERC, RDCPJ 531851-18).

Institutional Review Board Statement: Not applicable.

Informed Consent Statement: Not applicable.

Data Availability Statement: The datasets generated during the current study are available from the corresponding author on reasonable request.

Conflicts of Interest: The authors declare no conflict of interest.

References

1. González-Gutiérrez, J.; Stringari, G.B.; Emri, I. *Powder Injection Molding of Metal and Ceramic Parts*; IntechOpen: London, UK, 2012; pp. 65–88.
2. Heaney, D.F. *Handbook of Metal Injection Molding*, 2nd ed.; Woodhead Publishing: Cambridge, UK, 2019; pp. 1–656.
3. Sulong, A.B.; Muhamad, N.; Arifin, A.; Yong, K.B. Optimizing injection parameter of metal injection molding processes using the feedstock of 16 μm stainless steel powder (SS316L), PEG, PMMA and stearic acid. *J. Appl. Sci. Res.* **2012**, *8*, 2998–3003.
4. Demers, V. Low-pressure powder injection moulding review: Enabling cost effective low and high volume PIM production, *Powder Inject. Mould. Int.* **2019**, *13*, 53–63.
5. German, R.; Bose, A. *Injection Molding of Metals Ceramics*; Metal Powder Industries Federation: Princeton, NJ, USA, 1997; pp. 1–413.
6. Costa, C.A.; Pasquali, F.M. Application of rapid tooling and rapid prototyping in low pressure injection molding process of ceramic parts. In Proceedings of the International Conference on Polymers and Moulds Innovations—PMI2014, Guimaraes, Portugal, 10–12 September 2014.
7. Pompe, R.; Brandt, J. Goceram's Medpimould technology offers cost-effective PIM production. *Met. Powder Rep.* **2001**, *56*, 14–17. [[CrossRef](#)]
8. Zampieron, J.V.; Soares, J.P.; Mathias, F.; Rossi, J.L.; Ambrozio Filho, F. Low Pressure Powder Injection Moulding of Stainless Steel Powders. *Key Eng. Mater.* **2001**, *189*, 610–615. [[CrossRef](#)]
9. Mangels, J.A.; Williams, R.M. Injection Molding Ceramics to High Green Densities. *Am. Ceram. Soc. Bull.* **1983**, *62*, 601–606.
10. Peltsman, M.I.; Peltsman, I.D. Low Pressure Hot Molding Machine. U.S. Patent 4416603, 22 November 1983.
11. Mangels John, A. Low-pressure injection molding. *Am. Ceram. Soc. Bull.* **1994**, *73*, 37–41.
12. Goncalves, A.C. Metallic powder injection molding using low pressure. *J. Mater. Process. Technol.* **2001**, *118*, 193–198. [[CrossRef](#)]
13. Quevedo Nogueira, R.E.F.; Bezerra, A.C.; dos Santos, F.C.; de Sousa, M.R.; Acchar, W. Low-Pressure Injection Molding of Alumina Ceramics Using a Carnauba Wax Binder: Preliminary Results. *Key Eng. Mater.* **2001**, *189*, 67–72. [[CrossRef](#)]
14. Piotter, V.; Bauer, W.; Knitter, R.; Mueller, M.; Mueller, T.; Plewa, K. Powder injection moulding of metallic and ceramic micro parts. *Microsyst. Technol.* **2011**, *17*, 251–263. [[CrossRef](#)]
15. Çetinel, F.A.; Bauer, W.; Knitter, R.; Haußelt, J. Factors affecting strength and shape retention of zirconia micro bending bars during thermal debinding. *Ceram. Int.* **2011**, *37*, 2809–2820. [[CrossRef](#)]

16. Medvedovski, E.; Peltsman, M. Low pressure injection moulding mass production technology of complex shape advanced ceramic components. *Adv. Appl. Ceram.* **2013**, *111*, 333–344. [[CrossRef](#)]
17. Sardarian, M.; Mirzaee, O.; Habibolahzadeh, A. Influence of injection temperature and pressure on the properties of alumina parts fabricated by low pressure injection molding (LPIM). *Ceram. Int.* **2017**, *43*, 4785–4793. [[CrossRef](#)]
18. Atre, S.V.; Park, S.J.; Zauner, R.; German, R.M. Process simulation of powder injection moulding: Identification of significant parameters during mould filling phase. *Powder Metall.* **2007**, *50*, 76–85. [[CrossRef](#)]
19. Muangwaeng, B.; Rojananan, S.; Rojananan, S. The Effect of Injection Parameters on Morphology in Metal Injection Moulding. *Adv. Mater. Res.* **2013**, *802*, 174–178. [[CrossRef](#)]
20. Walcher, H.; Knöpfle, C.; Maetzig, M. *Influence of Process Parameter on the Quality of MIM Parts, European Congress and Exhibition on Powder Metallurgy*; The European Powder Metallurgy Association: Shrewsbury, UK, 2016.
21. Huang, M.S.; Hsu, H.C. Influence of injection moulding and sintering parameters on properties of 316L MIM compact. *Powder Metall.* **2011**, *54*, 299–307. [[CrossRef](#)]
22. Amin, S.Y.M.; Muhamad, N.; Jamaludin, K.R. Optimization of Injection Molding Parameters for WC-Co Feedstocks. *J. Teknol.* **2013**, *63*, 51–54.
23. Askari, A.; Momeni, V. Rheological investigation and injection optimization of Fe–2Ni–2Cu feedstock for metal injection molding process. *Mater. Chem. Phys.* **2021**, *271*, 124926. [[CrossRef](#)]
24. Yang, S.; Zhang, R.; Qu, X. Optimization and evaluation of metal injection molding by using X-ray tomography. *Mater. Charact.* **2015**, *104*, 107–115. [[CrossRef](#)]
25. Sardarian, M.; Mirzaee, O.; Habibolahzadeh, A. Numerical simulation and experimental investigation on jetting phenomenon in low pressure injection molding (LPIM) of alumina. *J. Mater. Process. Technol.* **2017**, *243*, 374–380. [[CrossRef](#)]
26. Ben Trad, M.A.; Demers, V.; Dufresne, L. Effect of Powder Shape and Size on Rheological, Thermal, and Segregation Properties of Low-Pressure Powder Injection Molding Feedstocks. *J. Mater. Eng. Perform.* **2019**, *28*, 5551–5562. [[CrossRef](#)]
27. *ASTM B923-16*; Standard Test Method for Metal Powder Skeletal Density by Helium or Nitrogen Pycnometry. ASTM International: West Conshohocken, PA, USA, 2016.
28. *ASTM D3418-15*; Standard Test Method for Transition Temperatures and Enthalpies of Fusion and Crystallization of Polymers by Differential Scanning Calorimetry. ASTM International: West Conshohocken, PA, USA, 2015.
29. *ASTM E1269-11*; Standard Test Method for Determining Specific Heat Capacity by Differential Scanning Calorimetry. ASTM International: West Conshohocken, PA, USA, 2011.
30. *ASTM D5930-17*; Standard Test Method for Thermal Conductivity of Plastics by Means of a Transient Line-Source Technique. ASTM International: West Conshohocken, PA, USA, 2017.
31. Lamarre, S.G.; Demers, V.; Chatelain, J.-F. Low-pressure powder injection molding using an innovative injection press concept. *Int. J. Adv. Manuf. Technol.* **2017**, *91*, 2595–2605. [[CrossRef](#)]
32. Lamarre, S.G.; Demers, V.; Chatelain, J.-F. A Low-Pressure Powder Injection Molding Machine and Method. U.S. Patent 10,919,092, 16 February 2021.
33. Ilinca, F.; Héту, J.-F.; Derdoufu, A.; Stevenson, J. Metal injection molding: 3D modeling of nonisothermal filling. *Polymer Eng. Sci.* **2002**, *42*, 760–770. [[CrossRef](#)]
34. Demers, V.; Fareh, F.; Turenne, S.; Demarquette, N.R.; Scalzo, O. Experimental study on moldability and segregation of Inconel 718 feedstocks used in low-pressure powder injection molding. *Adv. Powder. Technol.* **2018**, *29*, 180–190. [[CrossRef](#)]
35. Malkin, A.I.; Isayev, A.I. *Rheology: Concepts, Methods, and Applications*, 4th ed.; ChemTec Publishing: Ontario, CA, USA, 2022.
36. Poh, L.; Della, C.; Ying, S.; Goh, C.; Li, Y. Powder distribution on powder injection moulding of ceramic green compacts using thermogravimetric analysis and differential scanning calorimetry. *Powder Technol.* **2018**, *328*, 256–263. [[CrossRef](#)]
37. Thornagel, M.; Schwittay, V.; Hartmann, G. Powder-binder segregation: PIM-simulation at breakthrough. In Proceedings of the Euro PM 2014 International Conference and Exhibition, European Powder Metallurgy Association (EPMA), Salzburg, Austria, 21–24 September 2014.

Disclaimer/Publisher’s Note: The statements, opinions and data contained in all publications are solely those of the individual author(s) and contributor(s) and not of MDPI and/or the editor(s). MDPI and/or the editor(s) disclaim responsibility for any injury to people or property resulting from any ideas, methods, instructions or products referred to in the content.